INSTITUTE OF PHYSICS PUBLISHING JOURNAL OF PHYSICS D: APPLIED PHYSICS

J. Phys. D: Appl. Phys. **38** (2005) 1750–1759 doi:10.1088/0022-3727/38/11/016

Optical and RF electrical characteristics of atmospheric pressure open-air hollow slot microplasmas and application to bacterial inactivation

R Rahul[1], O Stan[1], A Rahman[1], E Littlefield[1], K Hoshimiya[1], A P Yalin[2], A Sharma[1], A Pruden[3], C A Moore[1], Z Yu[1] and G J Collins[1,4]

[1] Department of Electrical and Computer Engineering, Colorado State University, Fort Collins, CO 80523, USA
[2] Department of Mechanical Engineering, Colorado State University, Fort Collins, CO 80523, USA
[3] Department of Civil Engineering, Colorado State University, Fort Collins, CO 80523, USA

E-mail: gcollins@engr.colostate.edu

Received 1 December 2004, in final form 30 March 2005
Published 20 May 2005
Online at stacks.iop.org/JPhysD/38/1750

Abstract

We report electrical properties of radio frequency (RF)-driven hollow slot microplasmas operating in open air but with uniform luminous discharges at RF current densities of the order of A cm^{-2}. We employ interelectrode separations of 100–600 μm to achieve this open-air operation but because the linear slot dimension of our electrode designs are of extended length, we can achieve, for example, open-air slot shaped plasmas 30 cm in length. This creates a linear plasma source for wide area plasma driven surface treatment applications. RF voltages at frequencies of 4–60 MHz are applied to an interior electrode to both ignite and sustain the plasma between electrodes. The outer slotted electrode is grounded. Illustrative absolute emission of optical spectra from this source is presented in the region from 100 to 400 nm as well as total oxygen radical fluxes from the source. We present both RF breakdown and sustaining voltage measurements as well as impedance values measured for the microplasmas, which use flowing rare gas in the interelectrode region exiting into open air. The requirement for rare gas flow is necessary to get uniform plasmas of dimensions over 30 cm, but is a practical disadvantage. In one mode of operation we create an out-flowing afterglow plasma plume, which extends 1–3 mm from the grounded open slot allowing for treatment of work pieces placed millimetres away from the grounded electrode. This afterglow configuration also allows for lower gas temperatures impinging on substrates, than the use of active plasmas. Work pieces are not required to be part of any electrical circuit, bringing additional practical advantages. We present a crude lumped parameter equivalent circuit model to analyse the effects of changing RF sheaths with frequency of excitation and applied RF current to better understand the relative roles of sheath and bulk plasma behaviour observed in electrical characteristics. Estimates of the bulk plasma densities are also provided. Finally, we present results of afterglow plasma based bacteria inactivation studies (*Escherichia coli, Bacillus atrophaeus* and *B. atrophaeus* spores) in which we employ the flowing afterglow plume from a hollow slot microplasma device rather than the active plasma itself, which is fully contained between electrodes.

(Some figures in this article are in colour only in the electronic version)

[4] Author to whom any correspondence should be addressed.

1. Introduction

The development of plasma sources operating at atmospheric pressures is a recent trend in plasma engineering [1]. In certain applications, vacuum operation is required for control of gaseous species and to obtain optimal surface properties. On the other hand, non-vacuum plasma operation may enable a variety of processes at lower cost, allow new processes for work pieces that are not vacuum compatible and extend existing plasma methods to sealed gas systems that operate in mixtures of precursor gases at atmospheric pressure. In particular, glow discharges at atmospheric pressure are of interest for surface modification [2–5], thin film deposition [6, 7], surface cleaning [8], biomaterial decontamination [9] and sterilization [5, 10–18] as well as automotive [19, 20] applications. The efficacy of plasmas in this broad range of applications is largely due to their capability of producing large amounts of chemically reactive species, molecular fragments and energetic visible/UV/VUV photons.

Our research focuses on radio frequency (RF) driven open-air slot microplasmas comprising interelectrode plasma as well as flowing afterglow plasma. The powered wedge electrode is recessed within a volume behind the grounded slot (see figure 1) as is much of the associated interelectrode plasma, so that (external) work pieces require no electrical connection or vacuum. This close-coupled plasma-electrode design facilitates surface phenomena, such as cold emission of electrons from surfaces crucial to stable plasma operation via photo- and ion-induced secondary emission. In this work, we present electrical characterizations of the RF-driven open-air microplasmas operating at atmospheric pressure and using argon or helium as feed gas (i.e. gas flow supplied between the electrodes). Flow of rare gases helps in both ignition and stabilization of these discharges. Attempts to ignite or operate the discharge in room air caused the plasma to be limited to 1–3 cm in length and encouraged the plasma to arc. It is known that the required $\boldsymbol{E}$ field is an order of magnitude higher for molecular gases to achieve appreciable secondary ionization in the volume, compared to rare gases [21]. It is, therefore, easier to obtain a self-sustained plasma in a rare gas rather than in air. The economic implications of this gas flow are a concern but this issue may be ameliorated by proper electrode and gas flow design in a given application. It should be noted that the gas flows used are a requirement of open-air operation and not operation of the plasma *per se*.

Measurements include RF voltage–current (V–I) curves and impedance (real and reactive) and phase characteristics, both at breakdown and under stable luminous glow operation. Parametric RF impedance studies are performed versus applied RF frequency (4, 13.56, 27.12 and 60 MHz). Based on these measurements, we perform circuit analysis to examine the electrical properties and decouple sheath from bulk plasma effects. Electron number density estimates are presented. We also describe proof-of-principle experiments showing the potential utility of the slot microplasma for biological inactivation.

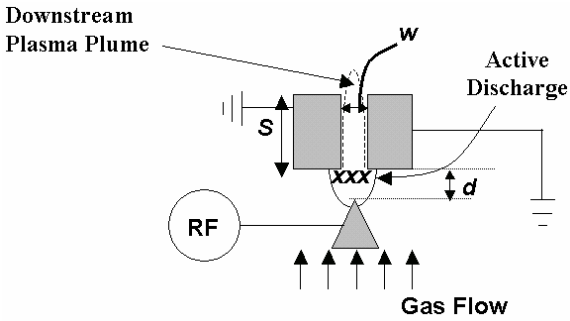

Figure 1. Schematic diagram of RF driven hollow slot micro-discharge. The recessed wedge electrode is actively powered with RF while the slot electrode is grounded.

2. Slot microplasma design and operating conditions

The present research focused on RF driven microplasmas comprised of a powered wedge-shaped electrode surrounded by grounded surfaces, acting as the other electrode (see figure 1). This electrode design allows for corona-initiated ignition in the confined region between the wedge tip and grounded slot. As shown in figure 1 gas is introduced at the bottom and flows through the electrodes into open air. The diagram shows critical electrode dimensions $w = 50$–$800\,\mu$m (slot width), $d = 100$–$600\,\mu$m (wedge to grounded slot interelectrode spacing). The wedge and slot electrodes are variable from 1 to 30 cm in length (dimension into page) creating a 'push-broom' source of photons, radicals and ions, all of which can impinge on an electrically floating work piece placed in several millimetre proximity of the grounded slot electrodes [22].

In addition to the interelectrode plasma contained in this interelectrode volume, a separate afterglow plume is formed, which extends out beyond the grounded slot for work piece irradiation. The open slot width (w in figure 1) was fixed at $200\,\mu$m for current studies and the interelectrode spacing (d in figure 1) was fixed at $400\,\mu$m. The length of the electrode along the slot is approximately 7.5 cm (3″) for the electrode system typically studied herein, but 30 cm long devices have been demonstrated [22]. The powered and slot electrodes were water-cooled. The former is copper while the latter is aluminium.

Experiments were performed at an ambient pressure of 89 kPa (open air in Colorado) using flow rates of 1–20 SLPM of industrial grade helium or argon gas as feed gas. While these high flow rates may slightly increase the pressure locally in the interelectrode volume, we observed no discernable difference in current–voltage (I–V) characteristics for argon flows of 3–13 SLPM. The use of rare gases as feed gas is critical to stable ignition and operation, although we recognize that their use increases operating expenses. For 13.56 MHz operation at these argon flows, we found that the non-equilibrium discharges in the slot were diffuse and non-filamentary for currents up to ∼1.5 A, per cm of slot length. At this current level, estimates of plasma parameters in the interelectrode region are as follows: pd ∼ 10 Torr cm, average rms $E \sim 4\,\mathrm{kV\,cm^{-1}}$, average rms $E/N \sim 20$ Td, average current density $\sim 0.3\,\mathrm{A\,cm^{-2}}$, associated power density

($E J \cos\Theta$) $\sim$1 kW cm^{-3} and energy per volume delivered to the flowing gas $\sim$100–200 J L^{-1}. In this regime, V–I curves showed that the voltage was approximately constant with increasing current. At higher currents, we observed the onset of glow-to-arc instabilities, without the appearance of any abnormal glow region. Depending on operating conditions, a plasma afterglow plume may protrude up to 3 mm from the slot.

The studies herein were at applied RF frequencies of 4, 13.56, 27.12 and 60 MHz, with up to 400 W of delivered power, and operating voltages of up to 400 V (rms) measured at the electrodes using a tuned measurement system (Z-Scan, Advanced Energy, Fort Collins, CO). Temporal measurements were made (and operation of the Z-Scan was verified) using a high voltage probe and a Pearson current transformer. A conventional LC matching network was used to impedance match the RF power generator to active plasmas.

3. Electrical characteristics

To better understand the slot microplasma discharge we analyse its electrical properties measured at the powered electrode. Specifically, we measure instantaneous and time-averaged (rms) voltage at the electrode, and current through the electrode into the plasma. We apply these data to a highly simplified circuit model to infer trends and relative behaviour of plasma parameters with various conditions.

3.1. Temporal measurements of current and voltage

In figure 2 we show representative voltage and current waveforms after breakdown of the slot microplasma excited at 13.56 MHz in argon gas with an electrode gap (d) of 400 μm. Because the oscilloscope is not impedance matched to the high voltage and current probes, we have phase corrected the raw data obtained from the oscilloscope to obtain the correct pre- and post-breakdown waveforms. We assumed here that prior to breakdown the electrode system is purely capacitive (I–V phase difference of 90°).

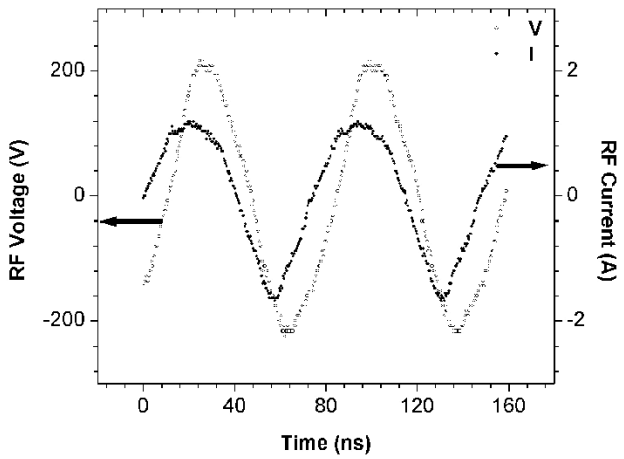

Figure 2. Post-breakdown temporal $I(t)$ and $V(t)$ waveforms for the slot microplasma device illustrating mixed resistive and capacitive behaviour. Conditions are: RF frequency of 13.56 MHz, interelectrode spacing of 400 μm and argon gas flow rate of $\sim$15 SLPM.

It can be seen in figure 2 that the phase between current and voltage is <90°, indicating the presence of both a resistive bulk plasma and a capacitive sheath. In these studies, we observed a reduction in the phase angle between current and voltage as the excitation frequency was increased from 13.56 to 60 MHz (the plasma becomes more reactive). This reduction in the phase was non-linear: for example, at an applied RF current value of 1 A the measured phase values for an argon plasma were −39°, −72° and −79° for 13.56 MHz, 27.12 MHz and 60 MHz, respectively, while, for helium plasma the values were −11°, −27°, −45° and −71° for applied RF frequencies of 4 MHz, 13.56 MHz, 27.12 MHz and 60 MHz, respectively. The phase variation versus RF current is presented in figure 3 and discussed below. The non-linear phase behaviour with the RF frequency implies that increasing the applied frequency causes the plasma to gain reactance and/or lose resistance, thus suggesting that the time-averaged RF sheath thickness and sheath area are changing in ways that require investigation.

However, separating out the relative contribution of sheath from bulk effects (capacitive versus resistive) is difficult. This analysis is complicated experimentally by (i) the fact that resistance and reactance calculations strongly depend on the measured I–V phase difference (which itself varies with current), and (ii) the error in phase measurement using non-resonant probes depends on signal magnitudes and the presence of harmonics. For these reasons we modified the apparatus to replace the voltage probe and current transformer with the Z-Scan tuned probe system, which makes time-averaged (rms) current, voltage and phase measurements and provides these and derivative measurements (resistance, reactance) through a serial interface to a computer. The remaining measurements discussed in this paper are all rms values.

3.2. Time-averaged measurements

The main operating regimes of the capacitive open-air slot discharge are illustrated in figure 3. The illustrative current–phase, I–V and current–power curves shown in the figure are for argon flow through the electrodes at an applied RF frequency of 13.56 MHz and an interelectrode gap spacing of 400 μm. Prior to ignition (region A $\rightarrow$ B), the RF voltage increases monotonically with the RF current. The slope of this part of the I–V curve reflects the high (and relatively uniform) impedance of the unignited open-air case. Owing to the (approximately) 90° phase shift, the real power delivered under these pre-breakdown conditions remains relatively uniform and near zero. Once the peak of the applied voltage reaches a suitable breakdown value (point B) a stable discharge is initiated and the voltage drops discontinuously (B $\rightarrow$ C). Gas ignition or breakdown occurs on a statistical basis and is attributed to a corona breakdown mechanism owing to the sharp edges of the wedge and the slot electrodes. The initial secondary electrons required for the breakdown are judged to be produced mostly by photons rather than by ion-induced secondary electron generation, since the ion flux is initially very small at atmospheric pressure (prior to sheath formation) [23].

After breakdown is achieved, the RF voltage is relatively constant (C $\rightarrow$ D), and/or can extend back to lower applied RF

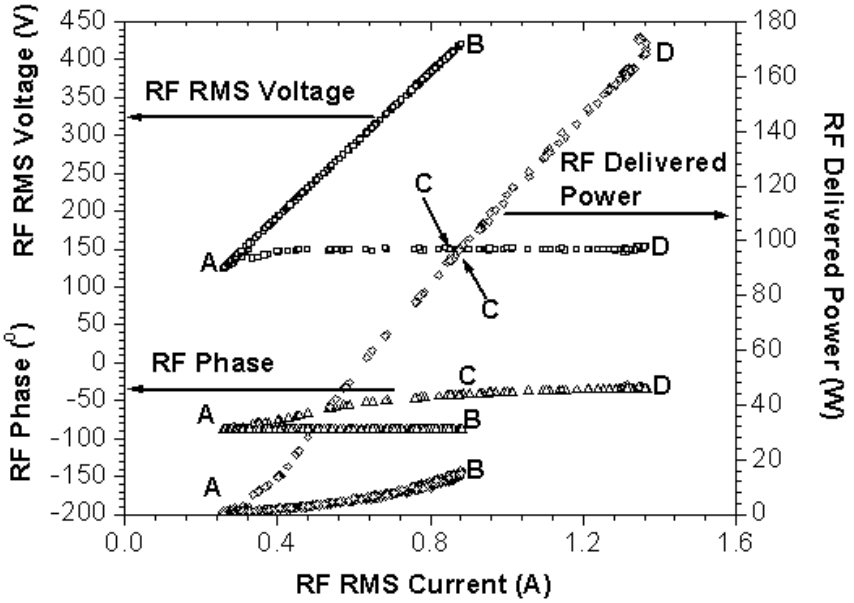

Figure 3. I–V, I–P and phase characteristics of the RF driven slot microplasma device showing pre- and post-breakdown behaviour. Conditions are: RF frequency of 13.56 MHz, interelectrode spacing of 400 μm and argon gas flow rate of ∼15 SLPM.

voltages in a hysteretic fashion (C → A) with the discharge being maintained. The constant voltage regime resembles a dc normal glow discharge operating at a potential significantly lower than the ignition voltage. As is evident from the figure, the voltage is independent of the current, which is high enough to sustain the discharge [24]. After breakdown, the real RF power delivered to the device increases dramatically (B → C) as the discharge changes from a purely capacitive discharge (pre-breakdown) to a partially resistive one. It is interesting to note here, that the RF delivered power before breakdown is not zero but although it is very small, it does have a certain finite value. We attribute this to the resistive losses in the electrode system. As the current is increased (C → D) the RF power increases and a hysteretic behaviour with current (power) decrease is also observed (C → A). For these operating conditions, we do not observe any transition to the abnormal glow or the arc mode for total RF currents below 0.3 A cm^{-1} (meaning 0.3 A delivered per 1 cm of slot length).

The phase characteristics of this open-air hollow electrode device are also shown in figure 3. The figure proves that our instantaneous measurements are correct and reliable wherein we get a pre-breakdown phase difference of approximately -90° (A → B). After breakdown (C) when a stable discharge is established between the electrodes the phase magnitude starts to decrease with current. This, along with the observed increase in the measured RF resistance (figure 4), forms the basis of the electrical modelling explained in section 3.3.

It is also informative to compare electrical impedance characteristics versus excitation frequency. Figure 4 shows this comparison for 13.56 and 60 MHz (for post-breakdown conditions). Prior to breakdown, the resistance is nearly negligible and the reactance is nearly constant. Once the gas breaks down and plasma is established between the two electrodes, the resistance and the reactance values start increasing with the applied RF current (though there is a subsequent decrease in the resistance for 13.56 MHz

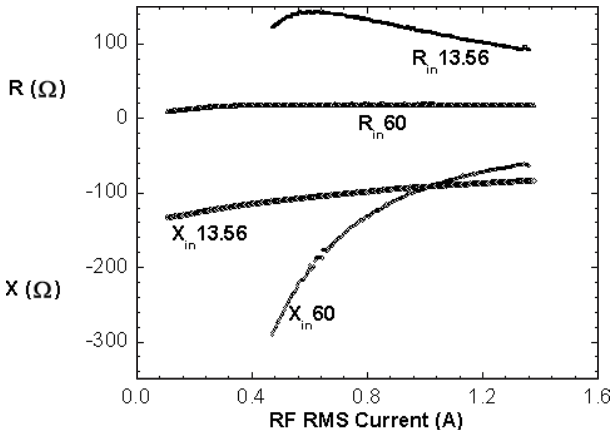

Figure 4. Resistance and reactance variation of the RF driven slot microplasma device versus RF current (post-breakdown). Conditions are: RF frequency of 13.56 and 60 MHz, interelectrode spacing of 400 μm and argon gas flow rate ∼ 15 SLPM. Note the factor of ten reduction in the bulk resistance at 60 as compared to 13.56 MHz.

excitation). This behaviour also illustrates the transition from a purely capacitive mode to a combined resistive/capacitive mode as the discharges transitions from pre- to post-breakdown. This post-breakdown behaviour corroborates the crude R–C electrical model explained latter.

3.3. Models of plasma sheath and bulk

Capacitive RF discharges will form capacitive sheath regions with relatively large electric fields consisting of both time-dependent (RF ac) and time-invariant (dc) components, and a resistive bulk region in the volume between the sheaths, which is characterized by the plasma density n_e and temperature T_e (electron energy distribution function). In our slot microplasma one sheath is formed along the

Figure 5. Crude equivalent lumped parameter circuit model of the post-breakdown mode of operation.

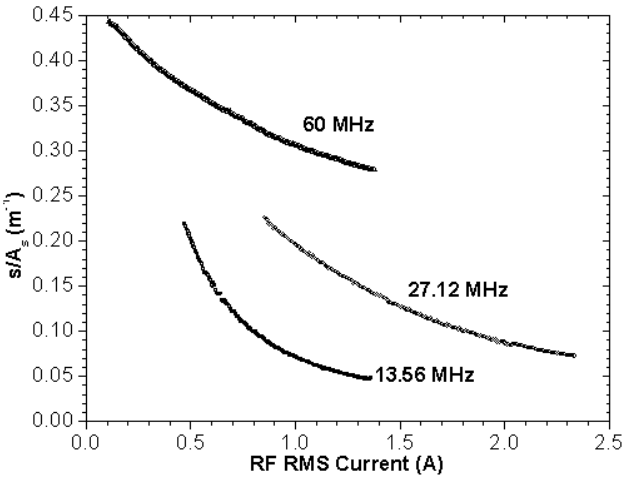

Figure 6. Calculated ratio of the RF sheath width s to the active electrode (sheath) area A_s of the RF driven slot microplasma device versus applied RF current. Conditions: applied RF frequencies of 13.56, 27.12 and 60 MHz, interelectrode spacing of 400 μm and argon gas flow rate of ∼15 SLPM.

wedge electrode near its apex, and a second sheath is expected along the grounded surfaces in close proximity to the powered wedge electrode. It is possible to model the plasma after breakdown in terms of linear and non-linear components [25, 26]. Thus, as shown in figure 5, the plasma is modelled as an equivalent series circuit consisting of a capacitor (powered electrode sheath), a resistor (bulk plasma) and a second capacitor (grounded electrode sheath). The two sheath regions are expected to behave similarly with changing conditions; therefore, we further simplify this circuit model to a series combination of a resistor R_B and a lumped capacitor C_s. We note that these simplifications may have an effect on the absolute magnitude of our calculations but still allow insight into relative behaviour with changing conditions. Moreover, this model is conducive to analysis of time-averaged data.

We can gain insight from our simple assumptive model by invoking physical models of the C_s and R_B components. First, we model the (combined) sheath capacitance as

$$C_s = \frac{\varepsilon_0 A_s}{2s}, \tag{1}$$

where ε_0 is the sheath permittivity, A_s the effective sheath area and s the sheath thickness. In this way, the reactance X_C of the plasma is directly proportional to the ratio of sheath thickness to sheath area (s/A_s). The effective sheath area is determined by the slot length (≈7.5 cm) in one dimension and an effective width near the apex of the powered wedge electrode in the other. Plotted in figure 6 is the experimental ratio s/A_s (found by analysing electrical data using equation (1)) for an argon flow between the electrodes and for applied RF frequencies of 13.56, 27.12 and 60 MHz. The plot shows that as the RF frequency increases, the s/A_s ratio increases, consistent with the plasma becoming more reactive.

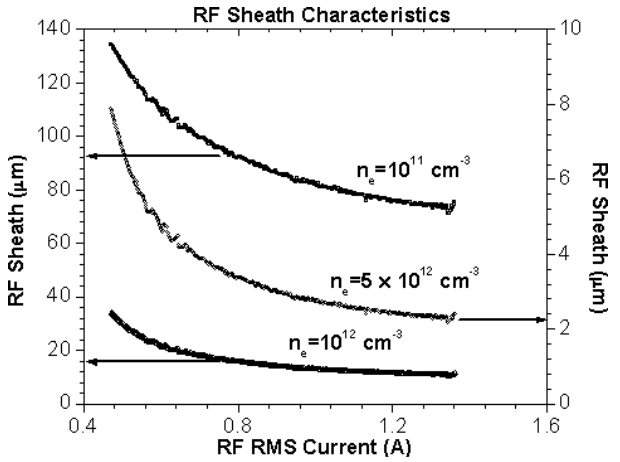

Figure 7. Calculated RF sheath widths using the RC approximation method. Electron densities are 10^{11}, 10^{12} and 5×10^{12} cm^{-3} and electron temperature 1 eV. Conditions are: applied RF frequency of 13.56 MHz and argon flow rate of ∼15 SLPM.

We also consider the plasma resistance measurements by assuming that all resistance is due to the bulk, which we express in the form

$$R_B = \frac{L}{A_s \sigma} = \frac{d - 2s}{A_s \sigma}, \tag{2}$$

where σ is the bulk plasma conductivity and we approximated L as being equal to the electrode gap d. We believe that at higher applied RF frequencies the discharge is dominated by secondary electrons created by ion collisions with the electrodes rather than photon-dominated processes. Assuming that the area, A_s, corresponding to the bulk resistance and the area A_s corresponding to the sheath reactance are equal, we multiply equations (1) and (2) to obtain

$$R \cdot C = (d - 2s)\frac{\varepsilon_0}{\sigma 2s}. \tag{3}$$

Solving for the sheath width s we get

$$s = \frac{d/2}{(e \cdot n_e \cdot \mu_e \cdot R \cdot C/\varepsilon_0) + 1}, \tag{4}$$

where μ_e is the electron mobility. Here, we adopt a value of 0.05 m^2 V^{-1} s^{-1} for argon [27]. Using this formula we make estimates of the RF sheath behaviour as a function of various parameters.

Figure 7 shows the RF sheath thickness calculated using equation (4) for argon flow between the electrodes at an applied RF frequency of 13.56 MHz. We have performed the calculations for assumed electron densities (n_e) of 10^{11}, 10^{12} and 5×10^{12} cm^{-3}. The corresponding Debye lengths are given by [28]

$$\lambda_D \text{ (cm)} = 743 \cdot \sqrt{\frac{T_e \text{ (eV)}}{n_e \text{ (cm}^{-3})}}, \tag{5}$$

where T_e is the electron temperature. At high currents, the calculated RF sheath dimension for an electron density of 10^{13} cm^{-3} is nearly 1 μm, smaller than the Debye length, which is several micrometres. Since the sheath cannot be smaller than the Debye length we estimate that $\sim 5 \times 10^{12}$ cm^{-3} is the approximate upper limit on the electron density. Figure 7 shows that, in this case, the sheath thickness slightly exceeds

Table 1. Prominent atomic emission lines. Fine structure not included.

Transition	Transition wavelength (nm)	Energy levels
(N) $2p^3\ ^4S^0$–$3s\ ^4P$	120	0.0–10.34
(N) $2p^3\ ^2D^0$–$3s\ ^2D$	124	2.38–12.36
(N) $2p^3\ ^2P^0$–$3s\ ^2D$	141	3.57–12.36
(N) $2p^3\ ^2D^0$–$3s\ ^2P$	149	2.38–10.68
(N) $2p^3\ ^2P^0$–$3s\ ^2P$	174	3.57–10.68

or is comparable to the Debye length (λ_D at 0.5 eV = 2.3 μm, λ_D at 1 eV = 3.3 μm). A reduction by a factor of two in the RF sheath dimensions versus RF current leads to high electric field values in the sheath ($\sim$20 kV cm^{-1}). Since the sheath thickness, s, decreases more rapidly than do changes in the sheath potential, this suggests that increasing the current or excitation frequency leads to increases in the sheath electric fields. These larger sheath fields will cause the secondary electrons emitted from electrode surfaces to enter the bulk plasma region with higher energies, and thus should be observable as preferential excitation of higher-energy transitions in optical emission spectra.

4. Optical characteristics

Our set-up and calibration procedure, as well as results of prior absolute optical emission measurements have been described previously [29, 30]. Numerous atomic and molecular transitions have been observed and analysed in the UV/VUV region. Atomic transitions (summarized in table 1) are prominent in the 100–200 nm region. In the 200–300 nm region NO gamma emission (NO ($A\,^2\Sigma^+, v'$–$X, ^2\Pi v''$)) is dominant. In the 300–400 nm region the dominant emission is from the 2nd positive system of N_2 ($N_2(C\,^3\Pi_u$–$B\,^3\Pi_g)$) and 1st negative system of N_2^+ ($N_2^+(B\,^2\Sigma_u^+$–$X\,^2\Sigma_g^+)$), while relatively weak emission from NH and OH is also present.

Here, our focus is on studying spectral changes as a function of applied RF frequency. Representative absolute UV/VUV optical emission spectra from the hollow slot microplasma driven by RF frequencies of 13.56 and 60 MHz are shown in figures 8 and 9 (for operation in helium with nitrogen addition). For all our measurements at 13.56 and 60 MHz, the RF delivered power was kept at a constant value ($\sim$100 W). Figure 8 shows that the intensities of the atomic nitrogen transitions in the 110–200 nm region exhibit a distinct increase for an RF frequency of 60 MHz as compared to 13.56 MHz. The increase of the atomic nitrogen emissions with RF frequency suggests an increase in mean electron energy as the upper states of these transitions are considered to be excited via electron impact processes [30].

Figure 9 also shows an increase of nitrogen second positive emission with increased RF frequency. The upper state $N_2(C)$ of the nitrogen second positive emission is judged to be populated through electron pooling mechanisms involving the metastable $N_2(A)$ (reaction (R1a)) as well as electron impact excitation of $N_2(A)$ or of the ground state $N_2(X)$ (reactions (R1b) and (R1c), respectively). We also observe that at 60 MHz the ratio of emission from the band from $v' = 1$ to the band from $v' = 0$ increases substantially (see

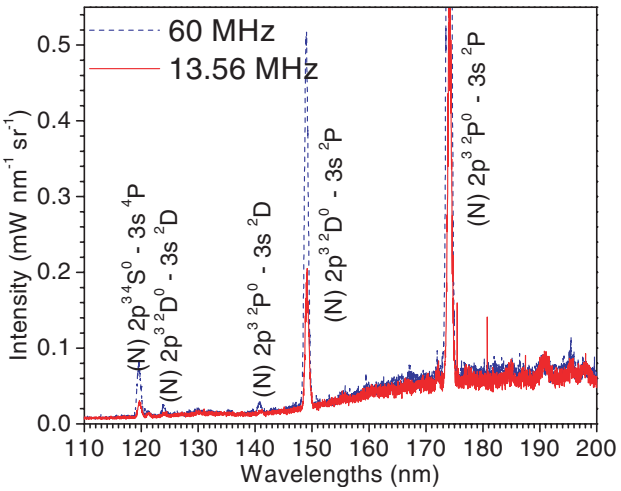

Figure 8. Spectra of slot microplasma in the 110–200 nm region for 13.56 and 60 MHz excitation. Helium flow rate and N_2 flow rates are 2 SLPM and 20 SCCM, respectively. Solid lines correspond to 13.56 MHz RF excitation (RF power 100 W) and dashed lines correspond to 60 MHz RF excitation. Emission is measured from 0.4 cm of slot length.

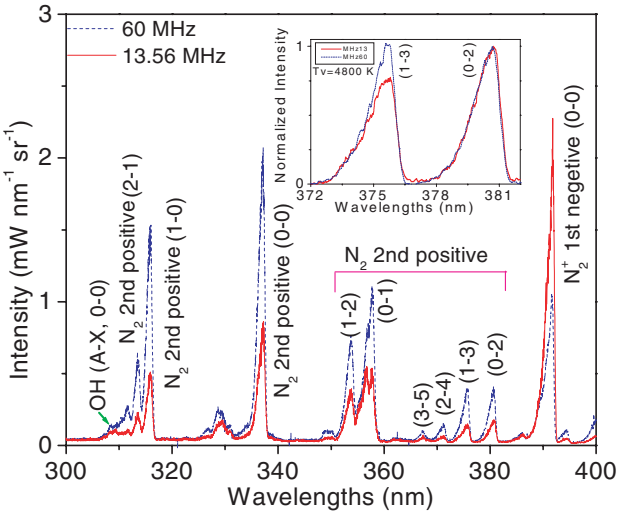

Figure 9. Spectra of slot microplasma in the 300–400 nm region for 13.56 and 60 MHz excitation. Helium flow rate and N_2 flow rates are 2 SLPM and 20 SCCM, respectively. Solid lines correspond to 13.56 MHz RF excitation (RF power 100 W) and dashed lines correspond to 60 MHz RF excitation. Emission is measured from 0.4 cm of slot length. Vibrational transitions are identified in parentheses. Inset shows normalized intensity of N_2 second positive (0–2) and (1–3) vibrational bands to highlight the population inversion between the $v' = 0$ and $v' = 1$ vibrational bands.

inset of figure 11). Past research has shown an inversion of these vibrational states associated with energy pooling of long lived metastable $N_2(A)$ states resulting in population of $N_2(C)$ states (reaction (R1a)) [31, 32]. Therefore, the observed increase in second positive intensity and the observed population inversion are probably due to increases in both electron impact excitation reactions (R1b) and (R1c) and energy pooling reactions (R1a), both of which suggest an

increase in electron energy (since $N_2(A)$ itself is formed from electron impact reactions).

$$N_2(A) + N_2(A) \rightarrow N_2(C) + N_2(X), \qquad (R1a)$$

$$N_2(A) + e\ (>4\,eV) \rightarrow N_2(C) + e, \qquad (R1b)$$

$$N_2(X) + e \rightarrow N_2(C) + e. \qquad (R1c)$$

In contrast to the $N_2(C)$ emissions, the $N_2^+(B–X)$ emission intensities decrease as the RF intensity is increased. For helium gas glows, excitation to the first negative systems of N_2^+ is predominantly due to charge transfer mechanisms by helium ions and helium dimer ions [33] and Penning ionization by helium metastables [32–34]. (Direct electron impact of $N_2(X)$ is thought to be negligible as energies of >15 eV would be required.) The decrease in intensity (with increase of RF frequency) of the first negative system may be due to a change in sheath effects and needs further investigation.

Owing to fast collisional relaxation at atmospheric pressure, the rotational temperature may be used as an accurate measure of the translational gas temperature. We have previously reported temperature measurements at 13.57 MHz based on the (0, 0) vibrational band of the second positive system of $N_2(C\,^3\Pi_g–B\,^3\Pi_g)$ in the vicinity of 337 nm [30]. The temperature measurement is performed by finding the best agreement between measured spectra and simulated spectra (produced using the spectral simulation tool SPECAIR) [35]. At both 13.57 and 60 MHz we find a rotational (gas) temperature of 650 ± 100 K. The temperature measurement is path-integrated (so that it cannot separate temperature in the plume and interelectrode regions) and suffers from some interference from the NH (0–0) band at 336 nm.

5. Applications—bacteria inactivation

5.1. Motivations

Traditional techniques for bacteria inactivation, like autoclaving and ethylene oxide treatment can be hazardous, time consuming and not suitable for heat sensitive materials or food packaging. Hence, an alternative method to inactivate bacteria is needed that is safe, convenient to operate and fast. Atmospheric pressure plasmas provide a means of microbial inactivation, which eliminate harmful gas emissions and make operation possible at high rates with reduced temperature. Moreover, operation at atmospheric pressure makes the process feasible for use in open air, which significantly reduces the cost.

Different groups have experimented with plasmas as a means of bacterial inactivation [16, 17, 36–40]. One research group has developed a one atmosphere uniform glow discharge plasma (OAUGDP) reactor in which the electrodes are housed in a container of dimensions $40 \times 35 \times 35$ cm. They achieved inactivation rates of 6 $\log_{10}$ with 5 min of exposure using *Escherichia coli* embedded in agar medium [37]. Another commercial system that employs plasma combined with hydrogen peroxide as the active mechanism of inactivation has recently become available. (Johnson and Johnson Advanced Sterilization Products (ASP) sells the STERRAD 50 sterilizer, which operates in a vacuum.)

Our approach is focused on open-air operation with wedge-open slot electrodes that are driven by RF at 13.56 MHz with a flow of rare gas through the electrodes forming an afterglow plume. The powered electrode is enclosed within a grounded but slotted electrode so the device may be handheld.

5.2. Microbial strains and preparations

E. coli cultures were grown on LB agar (Difco, Sparks, MD) for 2 days at 37°C prior to experimentation. Cells were subsequently transferred from the plate under sterile conditions to 250 ml of phosphate buffer solution (PBS, pH 7.0). The solution was serially diluted to the required concentration range. Five millilitres of the solution was filtered in triplicate for each dilution onto pre-sterilized filter membranes (0.45 μm mixed cellulose esters, 47 mm diameter) (Millipore, Pittsburgh, PA). Following filtration, the membranes were placed on sterile 10 ml petri dishes containing 9 ml LB agar. The petri dishes with the filter membranes in place on the LB agar were exposed to the afterglow plume emitted from the grounded hollow slot electrode for the required time. After the plasma treatment, the petri dishes were incubated at 37°C for one day prior to determining the resulting number of colony forming units (CFUs).

Bacillus atrophaeus. B. atrophaeus is a gram-positive bacterium and contains thicker cell walls than *E. coli. B. atrophaeus* is also a commonly used reference strain in sterilization experiments. The thicker layers of peptidoglycan in the cell walls of *B. atrophaeus* are considered to render the strain more resistant to sterilization than *E. coli. B. atrophaeus* was obtained from the American Type Culture Collection (ATCC, Manassas, VA) and grown under recommended conditions at 30°C. For the experiments, the cultures were maintained on LB agar plates. *B. atrophaeus* cells were prepared for experimentation as described above for *E. coli*.

B. atrophaeus spores. *B. atrophaeus* spores (ATCC No 9372) were in the form of strips (3.81 cm $\times$ 0.64 cm) commonly used for verifying autoclave efficiency. The strips were obtained from Raven Biological Laboratories, INC, NE. These strips were certified to have an average initial CFU count of 1.2×10^7. The experiment on the *B. atrophaeus* spores was conducted by exposing the test strips in triplicate lengthwise under the plasma slot for 1, 5 or 10 min on each side. The control strip was unexposed to the plasma. After exposure, the strips were immersed in 5 ml of sterile tryptic soy broth (TSB, Difco) in 10 ml glass culture tubes and maintained on a rotary shaker for 21 h at ambient temperature. Thereafter, the resulting broth was serially diluted and the turbidity was determined using a HACH (Loveland, CO) 2100 N turbidometer. The diluted solutions were also plated onto LB agar plates and grown for 24 h at 30°C to determine the resulting CFUs.

5.3. Results and discussion

It is widely believed that oxygen radicals have a strong germicidal effect [41, 42]. Thus, in our studies we judge that UV and VUV emission are not the only components that are responsible for inactivation. This flux of radicals is large in our work as supported by the measurements of

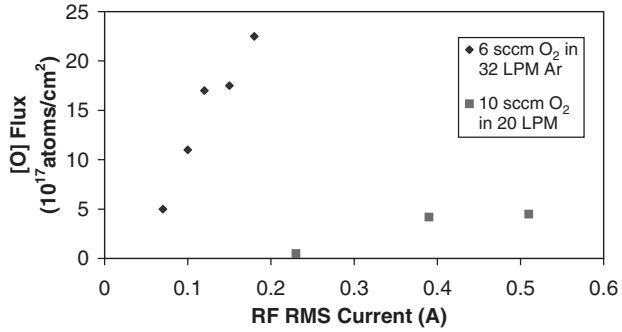

Figure 10. Total oxygen radical fluxes versus RF current in open-air slot plasma for two flow rates of oxygen added to the upstream argon flow through the slot plasma source.

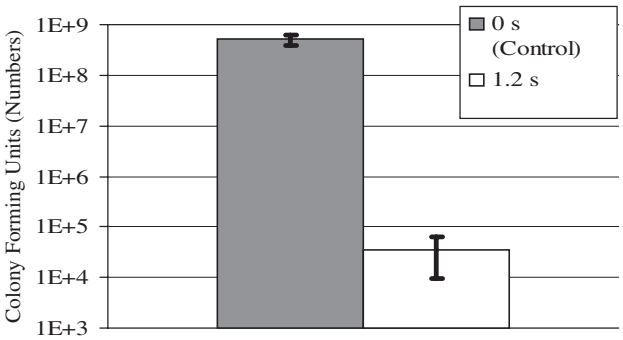

Figure 11. Log survivors of *E. coli* bacteria on LB agar after exposure to the afterglow plasma plume for several seconds.

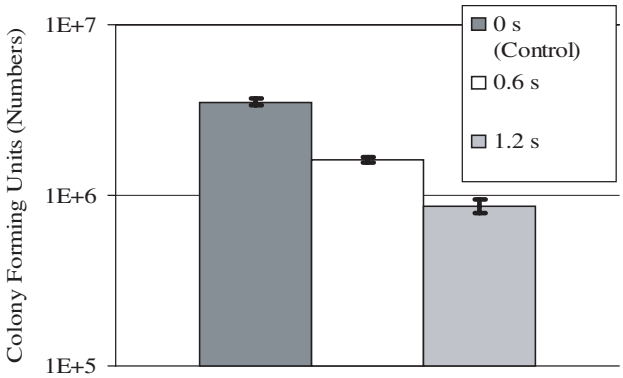

Figure 12. Log survivors of *B. atrophaeus* on LB agar after exposure to the afterglow plasma plume.

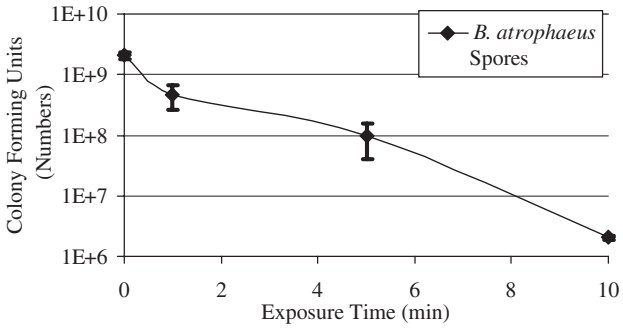

Figure 13. Survival curve of *B. atrophaeus* spores on LB agar after exposure to the plasma plume for tens of minutes.

the total oxygen radical flux density from the open-air slot plasma device, shown in figure 10. We measured the total oxygen radical concentration for the open-air slot microplasma device using a silver coated quartz crystal balance method [43]. We performed calibrations by oxygen gasification of known thickness of photoresist. In other words, we correlated the thickness of resist removed to the radical density, thereby determining the flux of radicals. This method could only determine the total radical flux with the atmospheric plasma operating. The relative distribution of individual oxygen reactive species, such as $O_2(a\,^1\Delta_g)$, O_2^- and atomic oxygen, could not be correctly obtained using this method alone. However, we have not conducted experiments wherein the samples would be exposed remotely to the plasma radials by shielding them from any UV radiation. All the data that have been presented for sterilization were from experiments wherein the samples were placed a few millimetres downstream of the grounded electrodes and both photon and radical irradiation occurred simultaneously. Since the distance of the irradiated samples from the slot reactor is relatively large compared to mean free paths, we conclude the samples are exposed by the afterglow and not directly by the active discharge. Photon irradiation arising from the active discharge plays an active role here. Our sterilization experiments have been performed in an open-air environment without any enclosed chamber making the process more convenient. It is noteworthy that the exposure time in our experiments is only 1 s to achieve five decades of inactivation. The plasma plume had a lethal effect on all microbes tested with a treatment time of about 1 s for non-sporulated forms. The effect of the plasma plume was also observed to differ with the kind of microbe tested. In figure 11 a comparison of control and plasma treated *E. coli* is shown. In this experiment, a reduction of almost 5 $\log_{10}$ was observed. The result of the *B. atrophaeus* experiment is shown in figure 12. Here, it was observed that *B. atrophaeus* was more challenging to inactivate, which was expected, considering the thicker cell walls. However, one log removal was observed in a little over 1 s exposure per unit area. The survival curve of the experiment on *B. atrophaeus* spores is shown in figure 13. Bacterial spores are considered to be one of the most difficult forms of bacteria to kill and are commonly used to test the efficiency of sterilization devices, such as autoclaves. An impressive 3 $\log_{10}$ removal of spores was observed with 10 min of exposure on each side of the spore strip.

The afterglow plume portion of the plasma was implemented for microbial inactivation, which is significantly different from using the active discharge. First, the afterglow plume temperature is less than 50°C, which is especially valuable for treating heat-sensitive samples. The active afterglow species at low temperature are less likely to harm temperature sensitive materials than the active discharge, which has a gas temperature of 500°C [30]. In the afterglow, there are fewer charged particles due to recombination processes within it, hence we judge that the afterglow plume consists primarily of neutral atoms, radicals and molecules as well as photons emerging from the active plasma. This greatly reduces the chance that the work piece surface would be damaged by positive ions accelerating in the floating sheath in front of the workpiece surface. Finally, the afterglow can fill

larger volumes than the active discharge present in the original slot between the electrodes, providing a larger active surface area and volume for surface treatment.

6. Conclusions

In conclusion, we demonstrated with our wedge-slot electrode designs that atmospheric plasmas could be generated with two micro-dimensions, the separation between electrodes (d) and the slot width (w). These two micro-dimensions were of the order of hundreds of micrometres, not tens of micrometres. With a wedge-slot electrode geometry the third electrode dimension may be of the order of tens of centimetres while maintaining a uniform diffuse plasma, more compatible with large area processing applications. However, the requirement of rare gas flow is a practical disadvantage. RF excitation from 1 to 60 MHz seems to better allow for arc free operation at current densities up to a few A cm^{-2}, over extended lengths as compared to dc operation. We note that the most temporally and spatially stable operation; lowest voltage operation; highest s/A values as well as lowest bulk plasma resistance occurred at 60 MHz, the highest frequency attempted to date. This indicates that this trend may extend into the near microwave region from 0.1 to 1 GHz. Finally, our wedge-open slot electrode design allows for creation of an extended (30 cm long and a few mm deep) afterglow region with low gas temperature into which we can immerse temperature sensitive work pieces for plasma-based treatments, without any required electrical connection.

Acknowledgments

This work is supported by the National Science Foundation and by Advanced Energy Industries Inc.

References

[1] Kunhardt E E 2000 Generation of large-volume, atmospheric-pressure, nonequilibrium plasmas *IEEE Trans. Plasma Sci.* **28** 189–200

[2] Kanazawa S 1989 Glow plasma treatment at atmospheric pressure for surface modification and film deposition *Nucl. Instrum. Methods Phys. Res.* **37–38** 842–5

[3] Okazaki S J and Kogoma M 1989 Glow discharge plasma at atmospheric pressure and its application *Proc. Japan. Symp. Plasma Chem.* **2** 95

[4] Carr A K 1997 Increase in the surface energy of metal and polymeric surfaces using the one atmosphere uniform glow discharge plasma (OAUGDP) *MS Thesis in Electrical and Computer Engineering* University of Tennessee, Knoxville

[5] Bogaerts A *et al* 2002 Gas discharge plasmas and their applications *Spectrochim. Acta* B-*At. Spectrosc.* **57** 609–58

[6] Kanazawa S *et al* 1988 Stable glow plasma at atmospheric pressure *J. Phys. D: Appl. Phys.* **21** 838–40

[7] Yokoyama T *et al* 1990 The improvement of the atmospheric pressure glow plasma method and the deposition of organic films *J. Phys. D: Appl. Phys.* **23** 374–7

[8] Roth J R 1999 Method and apparatus for cleaning surfaces with a glow discharge plasma at one atmosphere of pressure *US Patent* 5,938,854

[9] Kayes M M 2000 Inactivation of foodborne pathogens using a one atmosphere uniform glow discharge plasma. *MS Thesis in Department of Food Science and Technology* University of Tennessee, Knoxville

[10] Ku Y *et al* 1995 Sterilization of materials with a one atmosphere uniform glow discharge plasma in air *APS Bull.* **40** 1685

[11] Ku Y *et al* 1996 Sterilization of material with a one atmosphere uniform glow discharge plasma *Proc. 23rd IEEE International Conf. on Plasma Science (Boston, Massachusetts)* Paper 2IP-15

[12] Montie T C, Kelly-Wintenberg K and Roth J R 2000 An overview of research using a one atmosphere uniform glow discharge plasma (OAUGDP) for sterilization of surfaces and materials *IEEE Trans. Plasma Sci.* **28** 41–50

[13] Ben Gadri R *et al* 2000 Sterilization and plasma processing of room temperature surfaces with a one atmosphere uniform glow discharge plasma (OAUGDP) *Surf. Coat. Technol.* **131** 528–42

[14] Laroussi M 1995 Sterilization of tools and infectious waste by plasmas *Bull. Am. Phys. Soc.* **40** 1685–6

[15] Laroussi M 1996 Sterilization of contaminated matter with an atmospheric pressure plasma *IEEE Trans. Plasma Sci.* **24** 1188–91

[16] Laroussi M, Alexeff I and Kang W 2000 Biological decontamination by non-thermal plasmas *IEEE Trans. Plasma Sci.* **28** 184–8

[17] Laroussi M 2002 Non-thermal decontamination of biological media by atmospheric pressure plasmas: Review, analysis and prospects *IEEE Trans. Plasma Sci.* **30** 1409–15

[18] Laroussi M and Leipold F 2003 Plasma-based sterilization *Proc. Int. Conf. on Phenomenon in Ionized Gases* (*Greifswald, Germany*)

[19] Penetrante B M 1998 Plasma assisted catalytic reduction of NO_x *SAE Paper* 982508

[20] Hammer T 2000 Non thermal plasma treatment of automotive exhaust gases (Written under contract by Siemens AG, Corporate Technology)

[21] Aleksandrov V Y *et al* 1975 Self-sustained volume discharge at atmospheric pressure *Sov. Phys.—Tech. Phys.* **20** 62–5

[22] Yu Z *et al* 2003 Radio-frequency-driven near atmospheric pressure microplasma in a hollow slot electrode configuration *Appl. Phys. Lett.* **83** 854–6

[23] Druyvesteyn M J and Penning F M 1940 The mechanism of electrical discharges in gases at low pressure *Rev. Mod. Phys.* **12** 87–176

[24] Roth J R 1994 *Industrial Plasma Engineering Vol I Principles* (Bristol: Institute of Physics) pp 149–51

[25] Chen Z Y 2002 Impedance matching for one atmosphere uniform glow discharge plasma (OAUGDP) reactors *IEEE Trans. Plasma Sci.* **30** 1922–30

[26] Chen Z Y 2003 PSpice simulation of one atmosphere uniform, glow discharge plasma (OAUGDP) reactor systems *IEEE Trans. Plasma Sci.* **31** 511–20

[27] Schoenbach K H and Stark R H 1999 Direct current high pressure glow discharges *J. Appl. Phys.* **85** 2075–80

[28] Lieberman M A and Lichtenberg A J 1994 *Principles of Plasma Discharges and Materials Processing* (New York: Wiley)

[29] Yalin A P *et al* 2003 Electrical and optical emission characteristics of radio-frequency-driven hollow slot microplasmas operating in open air *Appl. Phys. Lett.* **83** 2766–8

[30] Rahman A *et al* 2004 Absolute UV and VUV emission in the 110–400 nm region from 13.56 MHz driven hollow slot microplasmas operating in open air *Plasma Sources Sci. Technol.* **13** 537–47

[31] Piper L G 1988 State-to-state $N_2(A\,^3\Sigma_u^+)$ energy pooling reactions. II. The formation and quenching of N_2(B 3Pig, $v' = 1$–12) *J. Chem. Phys.* **88** 6911–21

[32] Benedictis S D and Dilecce G 1995 Vibration relaxation of $N_2(C, v)$ state in n2 pulsed rf discharge; electron impact and pooling reactions *Chem. Phys.* **192** 149–62

[33] Pouvesle J M and Bouchoule A 1982 Modeling of the charge transfer afterglow excited by intense electrical discharges in

high pressure helium nitrogen mixtures *J. Chem. Phys.* **77** 817–25

[34] Pouvesle J M, Stevefelt J and Collins C B 1985 Study of two-body and three-body channels of the reaction of metastable helium atoms with nitrogen *J. Chem. Phys.* **82** 2274–9

[35] Laux C O 1993 Optical diagnostics and radiative emission of air plasmas; *PhD Thesis in Mechanical Engineering* Stanford University

[36] Kelly-Wintenberg K *et al* 1998 Room temperature sterilization of surfaces and fabrics with a one atmosphere uniform glow discharge plasma *J. Indust. Microbiol. Biotechnol.* **2** 69–74

[37] Kelly-Wintenberg K *et al* 1999 Use of a one atmosphere uniform glow discharge plasma (OAUGDP) to kill a broad spectrum of microorganisms *J. Vac. Sci. Technol. A—Vac., Surf. Films* **17** 1539–44

[38] Moisan M *et al* 2001 Low-temperature sterilization using gas plasmas: A review of the experiments and an analysis of the inactivation mechanisms *Int. J. Pharmaceutics* **226** 1–21

[39] Kelly-Wintenberg K *et al* 2000 Air filter sterilization using a one atmosphere uniform glow discharge plasma (the volfilter) *IEEE Trans. Plasma Sci.* **287** 64–71

[40] Roth J R *et al* 2000 A remote exposure reactor (RER) for plasma processing and sterilization by plasma active species at one atmosphere *IEEE Trans. Plasma Sci.* **28** 56–63

[41] Laroussi M 1996 Sterilization of contaminated matter with an atmospheric pressure plasma *IEEE Trans. Plasma Sci.* **24** 1188–991

[42] Laroussi M *et al* 1999 Images of biological samples undergoing sterilization by a glow discharge at atmospheric pressure *IEEE Trans. Plasma Sci.* **27** 34–5

[43] Yu Z *et al* 1991 Wide area near afterglow oxygen radical source used as a polymer resist asher *Appl. Phys. Lett.* **59** 1194–6